The Astrophysical Journal, 968:94 (9pp), 2024 June 20 https://doi.org/10.3847/1538-4357/ad4493

The Distance to the S147 Supernova Remnant

C. S. Kochanek[1,2], John C. Raymond[3], and Nelson Caldwell[3]
[1] Department of Astronomy, The Ohio State University, 140 West 18th Avenue, Columbus, OH 43210, USA
[2] Center for Cosmology and Astroparticle Physics, The Ohio State University, 191 W. Woodruff Avenue, Columbus, OH 43210, USA
[3] Harvard-Smithsonian Center for Astrophysics, 60 Garden Street, Cambridge, MA 02138, USA

Received 2024 March 20; revised 2024 April 22; accepted 2024 April 25; published 2024 June 14

Abstract

In the absence of a parallax distance to a pulsar or a surviving binary in a supernova remnant (SNR), distances to Galactic SNRs are generally very uncertain. However, by combining Gaia data with wide-field, multifiber echelle spectroscopy, it is now possible to obtain accurate distances to many SNRs with limited extinction by searching for the appearance of high-velocity Ca II or Na I absorption lines in hot stars as a function of distance. We demonstrate this for the SNR S147 using the spectra of 259 luminous blue stars. We obtain a median distance of 1.37 kpc (1.30–1.47 kpc at 90% confidence), which is consistent with the median parallax distance to the pulsar of 1.46 kpc (1.12–2.10 kpc at 90% confidence) but with significantly smaller uncertainties. Our distance is also consistent with the distance to the candidate unbound binary companion in this SNR, HD 37424 at a photogeometric distance of 1.45 kpc (1.40–1.50 kpc at 1σ). The presence of high-velocity absorption lines is correlated with the Hα/O [III] emission-line flux of the SNR but not with the radio flux.

Unified Astronomy Thesaurus concepts: Supernova remnants (1667); Interstellar line absorption (843); Distance measure (395)

Supporting material: machine-readable table

1. Introduction

Supernova remnants (SNRs) dominate the dynamics of the interstellar medium (ISM) and the chemical evolution of the Galaxy. They are physically interesting and important probes of both the explosion and nature of progenitor stars (see, e.g., the reviews of Vink 2012 and Dubner & Giacani 2015). For example, estimates of ejecta masses, velocities, and energies constrain the progenitor and explosions (e.g., Temim et al. 2022; Braun et al. 2023). They are laboratories for shock physics (e.g., Raymond et al. 2020a, 2020b). They can be searched for bound or unbound binaries after the explosion in both core collapse (e.g., Dinçel et al. 2015; Fraser & Boubert 2019; Kochanek et al. 2019; Kochanek 2021) and Type Ia remnants (e.g., Kerzendorf et al. 2009). Just as in extragalactic SNRs (e.g., Badenes et al. 2009; Jennings et al. 2014), the age distribution of the surrounding stellar population can be used to estimate the mass of the progenitor (Kochanek 2022).

A major challenge in using SNRs for any of these applications is determining their distances. Almost all Galactic SNR distances are significantly uncertain. The most common estimates use H I velocities or pulsar dispersion measures, neither of which are very precise. For our eventual target, S147 (Simeis 147, G180.0-1.7, the Spaghetti nebula), the traditional distance estimates range from roughly 0.8 to 2 kpc (see below in Section 3), leading to factor of 2.5 uncertainties in sizes or velocities from proper motions and a factor of 6 in luminosities or masses. Only three Galactic SNRs have distances from pulsar parallaxes: Vela (Dodson et al. 2003), the Crab (Lin et al. 2023, both VLBI and Gaia), and S147. The pulsar in S147, PSR J0538+2817, has a parallax of 0.72 ± 0.12 mas (Ng et al. 2007; Chatterjee et al. 2009), which corresponds to a median distance of 1.46 kpc (1.12–2.10 kpc at 90% confidence). There are also parallax distances to G039.7-02.0, G205.5+00.5 (Monoceros Loop), and G284.3-01.8 because they contain the interacting binaries SS 433 (see the review by Margon 1984), MWC 148 (Hinton et al. 2009), and 2MASS J10185560-5856459 (Corbet et al. 2011), respectively, and the donor stars have Gaia (Gaia Collaboration et al. 2016, 2023) parallaxes.[4]

Cha et al. (1999) demonstrated a new method for measuring SNR distances, looking for the appearance of high-velocity (up to several 100 km s^{-1}) Ca II and Na I absorption features from the SNR in the spectra of hot stars (which lack such features) superposed on the SNR as a function of distance. They estimated a distance to the Vela SNR of 250 ± 30 pc, which was later confirmed by the pulsar parallax distance of 286 ± 16 pc (Dodson et al. 2003). Interestingly, the high-velocity absorption features are also rapidly time variable in strength and wavelength (e.g., Kameswara Rao et al. 2020 most recently). The only other case where this approach has been deliberately used for distance determination is for the Cygnus Loop (Fesen et al. 2018, 2021; Ritchey et al. 2024).

There are many previous studies of absorption toward SNRs using small numbers of stars as probes of the properties of the SNR. For our target, S147, Silk & Wallerstein (1973) found high-velocity Ca II absorption in HD 36665. Phillips et al. (1981) and Phillips & Gondhalekar (1983) found high-velocity ultraviolet absorption lines in HD 36665 and HD 37318. Sallmen & Welsh (2004) found both high-velocity Ca II and Na I in these two stars and no high-velocity features in HD 37367. Sallmen & Welsh (2004) used distance estimates of 0.88, 1.38 (from Phillips et al. 1981) and based on the

---

[4] Curiously, the Gaia parallax for SS 433 of $\varpi = 0.118 \pm 0.023$ mas (geometric distance 6.4–8.5 kpc, photogeometric distance of 5.5–8.9 kpc; Bailer-Jones et al. 2021) is at best marginally consistent with estimates from kinematic models of its jets (e.g., 5.5 ± 0.2 kpc; Blundell & Bowler 2004).

magnitudes and colors of the stars) and $0.36^{+0.15}_{-0.09}$ kpc from Hipparcos (Perryman et al. 1997) for HD 36665, HD 37318, and HD 37367; they concluded that S147 had to be closer than 0.88 kpc in order for HD 36665 to lie behind it. Unfortunately, all of these distances were significantly wrong, including the Hipparcos parallax distance for HD 37367. Bailer-Jones et al. (2021) found (geometric) Gaia distances to these three stars of 1.37 kpc (1.32–1.44 kpc), 1.64 kpc (1.56–1.72 kpc), and 1.34 kpc (1.14–1.55 kpc).

Cha et al. (1999) depended on Hipparcos (Perryman et al. 1997) parallaxes and so could only investigate a very nearby SNR like Vela. With Gaia, it is possible to apply the method to tens of SNRs, as demonstrated by the Cygnus Loop result (Fesen et al. 2018, 2021), but both studies depended on observing stars one at a time, which led to either a very expensive program (∼70 stars for Vela) or a very sparse sample (6 in each study for Cygnus). Interestingly, only some background stars show high-velocity absorption features. It is not known if the existence of absorption is (anti)correlated with any observational property of the SNR (radio, emission lines, X-rays, etc.). Fortunately, there are now wide-field, multi-object, fiber-fed echelle spectrographs like Hectochelle on the MMT (Fabricant et al. 2005; Szentgyorgyi et al. 2011), M2FS on Magellan (Mateo et al. 2012), FLAMES on the Very Large Telescope (Pasquini et al. 2000), and HERMES on the Anglo-Australian Telescope (Sheinis 2016), which allow observations of tens to hundreds of stars simultaneously.

Here we demonstrate this approach using the MMT and Hectochelle to observe stars in the direction of S147. The 1° field of view of the fiber positioner is well matched to the 3° diameter (taken from Green 2019, although there are earlier measurements such as van den Bergh et al. 1973) of S147 and many other SNRs. Hectochelle can obtain 240 spectra at a resolution of 34,000 (~ 8 km s^{-1}) in 150 Å windows centered on Ca II $\lambda\lambda$3933.663, 3968.47 (H and K) or Na I $\lambda\lambda$5889.51, 5895.924 (D1, D2). We chose S147 as a demonstration case because the pulsar parallax (Ng et al. 2007; Chatterjee et al. 2009) provides a check of the method. S147 is also of interest because it contains the one fairly convincing example of a binary star, HD 37424, unbound in a supernova explosion (Dinçel et al. 2015; Kochanek 2021). We describe the selection of the stars and the observations in Section 2 and provide the observational results and analysis in Section 3. In Section 4 we summarize the results and discuss future applications.

2. Sample and Observations

We selected stars from Gaia DR3 (Gaia Collaboration et al. 2016, 2023) within 1°.7 of the center of the SNR (R.A. 84°.75, decl. 27°.83; Green 2009). They were also selected to have $G < 15$ mag and $\varpi > 0.2$ mas. We obtained estimates for the extinction toward each star using the three-dimensional `combined19 mwdust` models (Bovy et al. 2016), which are based on the Drimmel et al. (2003), Marshall et al. (2006), and Green et al. (2015) extinction distribution models. Figure 1 shows the distribution of the stars in extinction-corrected absolute magnitude and color simply using the inverse parallax for the distance. Superposed are solar metallicity PARSEC (Bressan et al. 2012; Marigo et al. 2013; Pastorelli et al. 2020) isochrones with ages of 10^7–10^9 yr in steps of 0.5 dex colored red for temperatures above 10^4 K. Also marked are the candidate unbound companion to the neutron star, HD 37424, and two stars, HD 36665 and HD 37318, previously known to show high-velocity Ca/Na absorption lines (Silk & Wallerstein 1973; Phillips et al. 1981; Phillips & Gondhalekar 1983; Sallmen & Welsh 2004). Dinçel et al. (2015) were concerned that these stars had distance estimates that could put them in the foreground of the SNR, but their Gaia parallaxes put them at or beyond the SNR distance (see Section 1; Kochanek 2021).

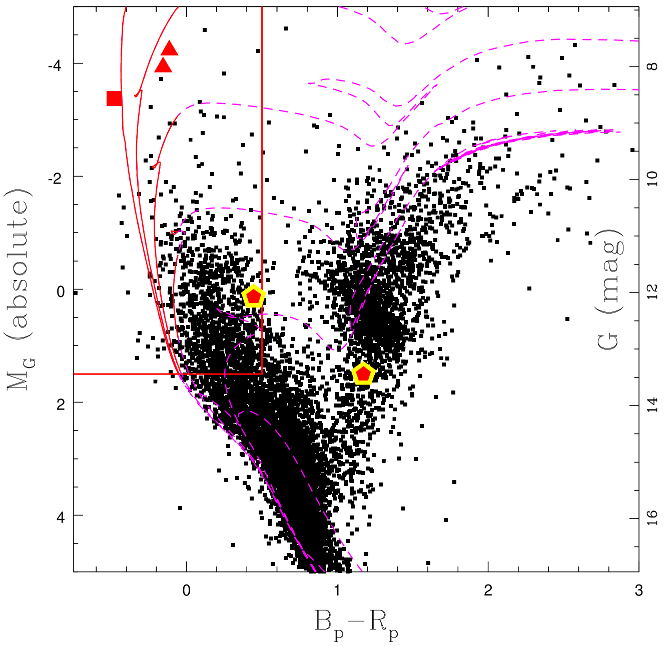

Figure 1. (Left): The distribution of the stars projected on S147 in absolute magnitude M_G and $B_P - R_P$ color after correcting for extinction. The vertical scale on the right is the corresponding apparent magnitude at the parallax distance of the pulsar. The curves are PARSEC isochrones from 10^7 to 10^9 yr in steps of 0.5 dex colored solid red (dashed magenta) for temperatures $>10^4$ K ($<10^4$ K). The red square is the candidate unbound binary companion, HD 37424, and the red triangles are two background stars, HD 36665 and HD 37318, with known high-velocity absorption lines. Stars in the upper left corner outlined by the red box are our high-priority targets. The yellow/red pentagons are the two stars whose spectra are shown in Figures 5 (bluer star) and 6 (redder star).

Stars hotter than roughly 10^4 K (i.e., O and B stars) do not have Ca II or Na I absorption (the coolest B stars can). These are the optimal targets to search for absorption lines from the ISM and the SNR. We selected as our primary targets stars with $M_G < 1.5$ mag and $B_P - R_P < 0.5$ mag, as shown in the red box in Figure 1. We also required total proper motions $\mu_{tot} <$ 10 mas yr^{-1}. Higher observational priorities were given to stars with parallaxes $0.4 < \varpi < 2.0$ mas as these should most strongly bracket the expected distance. Objects outside the box were included at still lower priorities. We divided the targets into Bright and Faint samples at $G < 11.5$ mag to help obtain similar counts over the large brightness range. The Bright sample was filled in with the lower priority $G > 13$ mag stars just to avoid having empty fibers.

We used the three pointings shown in Figures 2 and 3. One was centered on the 3° diameter SNR ("Center"), and the other two were centered contiguously to the southeast ("SE Edge") and northeast ("NE Edge") of the center to capture the edges, where we might expect lower velocities but higher projected column densities. Each was observed in two spectrograph configurations to cover both the Ca II and Na I wavelength ranges. We obtained a

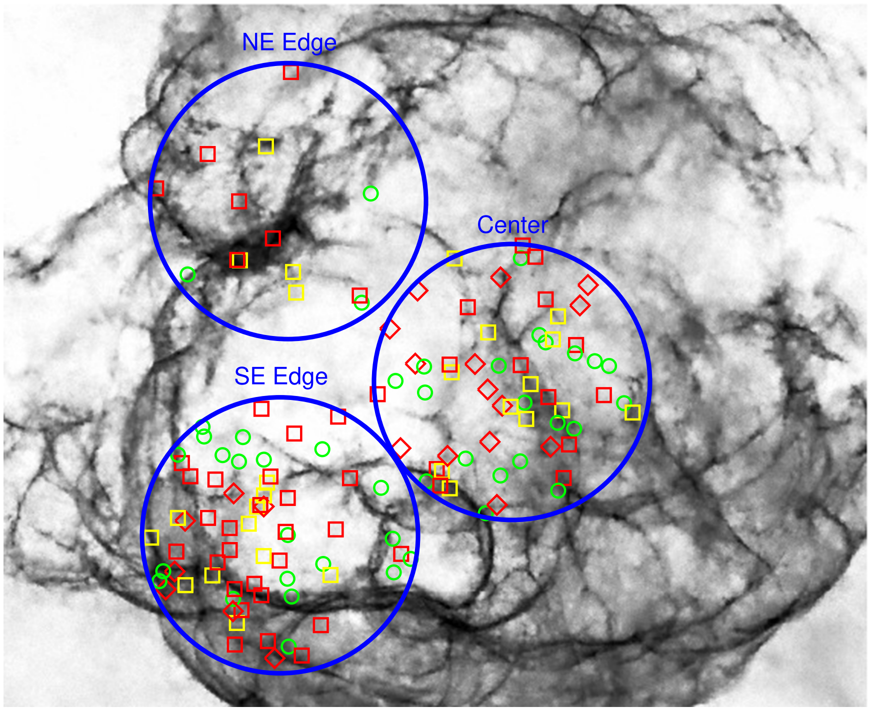

Figure 2. Background stars with both Na and Ca high-velocity absorption features (yellow squares), only one of Na (red diamonds) or Ca (red squares) high-velocity absorption features, or no high-velocity absorption features (green circles) superposed on the dual Hα/O [III] emission-line image of S147. The large blue circles are the three 1° diameter Hectospec fields. The full remnant is not shown to make the association of absorption with the Hα/O [III] emission easier to see.

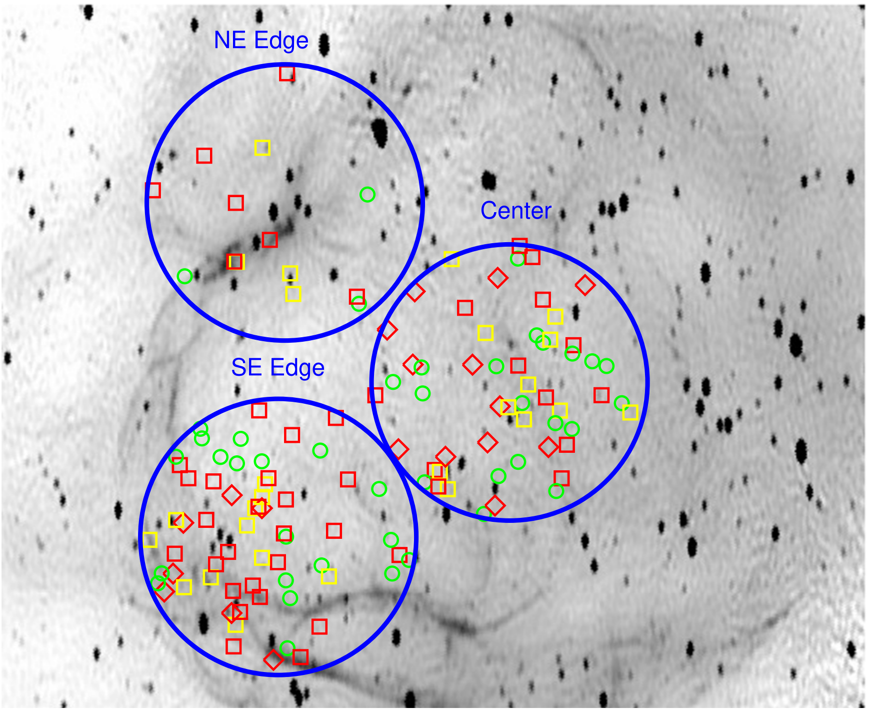

Figure 3. Background stars with both Na and Ca high-velocity absorption features (yellow squares), only one of Na (red diamonds) or Ca (red squares) high-velocity absorption features, or no high-velocity absorption features (green circles) superposed on the 1.4 GHz Canadian Galactic Plane Survey map of S147. The large blue circles are the three 1° diameter Hectospec fields. Stars too close to the radio point sources are not shown. The scale of this image is the same as that of Figure 2.

total of 11 observations. We obtained all 4 basic observations (Bright/Faint, Ca II/Na I) for the Center and SE Edge fields, plus 1 extra Bright Na I observation of the Center field. We only obtained the Bright Ca II/Na I observations for the NE Edge field. For the Faint observations, a star with $G \simeq 12.5$ mag had a signal-to-noise ratio (S/N) of ≃60 per pixel or ≃300 per resolution element. For the shorter exposure Bright fields, the same S/N was achieved for stars with $G \simeq 11$ mag. Table 1 summarizes the observations, where N_{spectra} is the number of stellar spectra obtained for each pointing.

Table 1
Field Information

Field/ Config	R.A.	Decl.	Line	Time (s)	N_{spectra}	G mag Range	UT Date
	(J2000)						
Center/Faint	05:39:08.4	+27:48:06.2	Ca II	9900	201	11.5–15	2023-09-26
Center/Faint	”	”	Na I	2160	203	11.5–15	2023-09-25
Center/Faint	”	”	Na I	2160	201	11.5–15	2023-11-09
Center/Bright	”	”	Ca II	2160	46	8.5–13	2023-11-04
Center/Bright	”	”	Na I	900	46	8.5–13	2023-11-04
SE Edge/Faint	05:42:55.9	+27:14:48.5	Ca II	9360	203	11.5–15	2023-09-27
SE Edge/Faint	”	”	Na I	3600	203	11.5–15	2023-10-12
SE Edge/Bright	”	”	Na I	900	56	8.5–13	2023-11-04
SE Edge/Bright	”	”	Ca II	2160	56	8.5–13	2023-11-04
NE Edge/Bright	05:42:49.1	+28:27:27.9	Na I	1080	46	8.5–13	2023-11-08
NE Edge/Bright	”	”	Ca II	2160	46	8.5–13	2023-11-24

The observations were processed using the standard IDL pipeline for Hectochelle data developed by the SAO Telescope Data Center (TDC[5]). Briefly, the separate CCD images are combined with cosmic-ray elimination, and the target traces are extracted to form 1D spectra. Wavelength calibration is supplied by ThAr exposures taken at the time of observation, and sky subtraction is performed using contemporaneous fiber spectra of blank regions within the 1° field. The wavelength stability of Hectochelle has been measured to be 0.78 ± 0.78 km s^{-1} over 3 yr, with an rms variation among fibers for a single pointing of just 0.17 km s^{-1} (P. Cargile 2024, private communication). In total, we obtained the spectra of 552 stars, of which 259 had $M_G < 1.5$ mag and $B_P - R_P < 0.5$ mag (the red box region of Figure 1), and 293 were either less luminous or redder. Of the 259 luminous blue stars, 172 (194) were good spectra showing clean Ca II (Na I) absorption lines, and 101 (60) of these stars had high-velocity absorption lines (heliocentric velocities outside 2 ± 10 km s^{-1}). The velocities of these clean absorption lines are shown in Figure 4 and listed in Table 2.

The spectra were individually examined to identify the velocities of the Ca II and Na I absorption features, which were flagged as being clean or not. Since equivalent widths, particularly with the complications of overlapping and weaker stellar and interstellar features, are unimportant for our present objectives, we simply measured line centroids. The Ca II absorption lines were generally stronger than the corresponding Na I absorption lines. The biggest distinction is simply between the luminous blue primary targets and the fainter or redder low-priority and filler targets. Figure 5 shows the spectra of a primary target near the lower (reddest) right (faintest) corner of the red selection box in Figure 1. The star has strong interstellar absorption near zero velocity and then strong Ca II lines near −86, −69, and +85 km s^{-1}. Only the −86 km s^{-1} line appears in the corresponding Na I spectrum. Figure 6 shows the spectra of a red giant star a little below the red clump in Figure 1. The low blue flux of the red giant leads to a very noisy Ca II spectrum. The Na I spectrum has a high S/N, but in addition to the interstellar Na I absorption, there is stellar Na I absorption plus additional stellar atmospheric absorption lines of other species. For these stars, high-velocity interstellar absorption can only be identified after modeling the spectrum to identify and remove these stellar features. For this paper we only use the luminous blue stars with clean absorption features.

3. Results

Figure 4 shows the velocities of the clean absorption components in the luminous blue stars as a function of parallax. There is a tight band at low velocities due to the ISM. Because S147 lies almost directly toward the Galactic anticenter, there is no systematic distance dependence on the ISM velocity relative to the Sun. If we roughly exclude the higher-velocity absorption lines, the median of the ISM velocity band is 2 km s^{-1}. For our standard models we will assign absorption lines within 2 ± 10 km s^{-1} to the ISM, although we report the consequences of different choices for the velocity width used to define the interstellar absorption. There are some higher-velocity features for stars closer than the pulsar of unknown origin, but there is a clear change in the numbers of high-velocity absorption components at the parallax of the pulsar, with velocities approaching ∼150 km s^{-1}. Kirshner & Arnold (1979) and Ren et al. (2018) found a similar velocity range for the emission lines from the SNR.

The goal is to determine the distance d_0 (in kpc) to the SNR, but we fit the measured parallaxes of the stars using $\varpi_0 = 1/d_0$. The property of the SNR is that it produces a change in the statistics of high-velocity absorption lines, so we model the probability of a star with distance $d > d_0$ ($d < d_0$) having a high-velocity absorption line as p_{far} (p_{near}). For a given distance, there are n_h (m_h) $d > d_0$ ($d < d_0$) stars with high-velocity absorption and n_l (m_l) without a high-velocity feature. The probability of the observed distribution is then

$$P(D|d_0, p_{\text{far}}, p_{\text{near}}) = p_{\text{far}}^{n_h}(1 - p_{\text{far}})^{n_l} p_{\text{near}}^{m_h}(1 - p_{\text{near}})^{m_l}. \quad (1)$$

Arguably, we should include the statistical weights so that

$$P(D|d_0, p_{\text{far}}, p_{\text{near}}) = \frac{(n_h + n_l)!(m_h + m_l)!}{n_h! n_l! m_h! m_l!} p_{\text{far}}^{n_h} \times (1 - p_{\text{far}})^{n_l} p_{\text{near}}^{m_h}(1 - p_{\text{near}})^{m_l}, \quad (2)$$

and we comment on the consequences of doing so below. We assume uniform priors of $0 \leqslant d_0 \leqslant 10$ kpc, $0 \leqslant p_{\text{far}} \leqslant 1$, and $0 \leqslant p_{\text{near}} \leqslant 1$ and use Bayesian methods to compute the final likelihood distributions. We include one additional elaboration to incorporate parallax uncertainties. For a star with parallax $\varpi_i \pm \sigma_i$ and a high-velocity absorption line, we make its

---

[5] https://lweb.cfa.harvard.edu/mmti/hectospec/hecto_pipe_report.pdf

Table 2
Absorption Velocities of the Hot Blue Stars

Gaia DR3 ID	Ca II (km s^{-1})	Na I (km s^{-1})	Gaia DR3 ID	Ca II (km s^{-1})	Na I (km s^{-1})
3441702193599182336	−118,4,38	2	3441703598051819776	3	2
3441706518633166080	⋯	−21,0	3441723496636807040	⋯	⋯
3441698860704616064	⋯	⋯	3442475974907331200	3	0
3442474561861744000	⋯	−13,0	3442449552266565888	3	5
3442476112346300800	3	2	3442452197968495616	−105,5	3
3442455011170611712	5	5	3442479337865371392	−32,1,87	−34,0
3442469751498370560	−127,2	3	3442472779451400448	3	0
3442491947889351296	3	4	3442491814744678528	⋯	5
3442546824687824256	0	3	3442506348915651328	5,23	2
3442599669964938368	−58,0	−14,−2	3442503527120074624	⋯	−24,1

Note. The entries are the velocities of the Ca II and Na I absorption lines separated by commas.

(This table is available in its entirety in machine-readable form.)

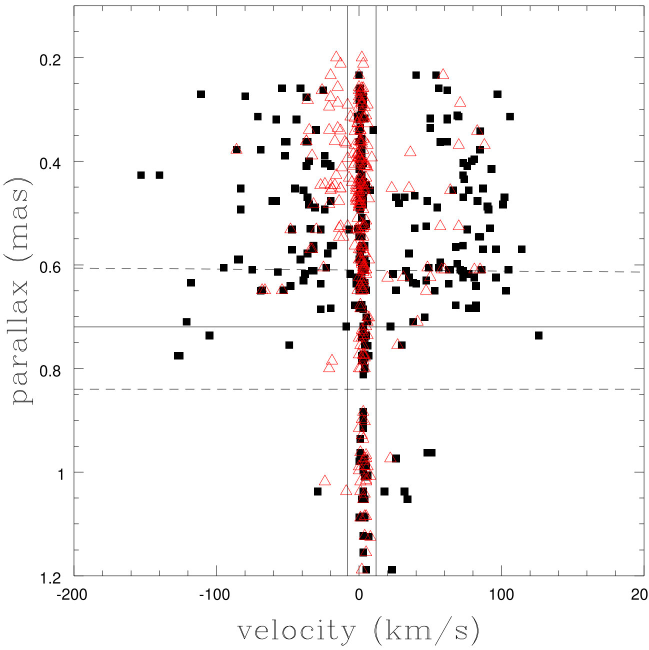

Figure 4. (Right): Heliocentric velocities of Ca II (black squares) and Na I (red triangles) absorption features as a function of parallax. Note that the parallax axis is inverted so that more distant stars are at the top. The horizontal lines show the pulsar parallax and its uncertainties. Absorption between the vertical lines at 2 ± 10 km s^{-1} is viewed as being due to the ISM for our standard model.

contribution to (for example) n_h be

$$\delta n_h = \frac{1}{\sqrt{2\pi}\,\sigma_i}\int_0^{\varpi_0} d\varpi \exp\left(-\frac{1}{2}\left(\frac{\varpi - \varpi_i}{\sigma_i}\right)^2\right) \tag{3}$$

and its contribution to m_h would then be $1 - \delta n_h$. This has the particular effect of down-weighting the importance of stars with large parallax errors.

Figure 7 shows the resulting estimates for the distance after marginalizing over the probabilities $p_{\rm far}$ and $p_{\rm near}$ of having a high-velocity absorption line. The results using only the Ca II, only the Na I, or both sets of absorption features give consistent results. The Na I results are significantly worse simply because fewer high-velocity Na I features were detected. The median distance estimates for Ca-only, Na-only, and both are 1.34, 1.47, and 1.37 kpc with 90% confidence regions of 1.28–1.43, 1.18–1.94, and 1.30–1.47 kpc, respectively. If we increase the width of the velocity window defining ISM absorption to 2 ± 15 km s^{-1} or 2 ± 20 km s^{-1}, the median distances are both 1.36 kpc with 90% confidence ranges of 1.29–1.45 kpc and 1.28–1.46 kpc, respectively, so the distance estimate is robust to changes in the definition of low and high velocities. Similarly, if we use Equation (2) instead of Equation (1), the median distances combining both lines for the three velocity ranges are 1.37, 1.35, and 1.36 kpc, with 90% confidence ranges of 1.31–1.43, 1.30–1.41, and 1.30–1.42 kpc, respectively, so this choices matters only at the level of ~0.01 kpc.

Figures 7 and 8 compare this estimate to a range of previous estimates. For the parallax of the pulsar ($\varpi = 0.72 \pm 0.12$ mas after combining Ng et al. 2007 and Chatterjee et al. 2009), the median distance is 1.46 kpc with a 90% range of 1.12–2.10 kpc. The candidate unbound binary star, HD 37424, has a geometric distance of 1.463 kpc (1.395–1.529 kpc at 1σ) and a photogeometric distance of 1.449 (1.399–1.501 kpc at 1σ) from Bailer-Jones et al. (2021), consistent with our estimate. The Bailer-Jones et al. (2021) uncertainties are 1σ rather than 90% confidence. Other estimates based on the ΣD radio surface brightness to diameter correlation (Clark & Caswell 1976; Kundu et al. 1980; Sofue et al. 1980; Guseinov et al. 2003), explosion models for the radius R (Kirshner & Arnold 1979; Kundu et al. 1980), extinction A_V (Fesen et al. 1985; Chen et al. 2017), or the pulsar dispersion measure (DM; Kramer et al. 2003) have given distances ranging from 0.6 to 1.9 kpc, as also shown in Figure 8, illustrating the challenge of determining the distances to SNRs. The Sallmen and Welsh (2004) upper limit of 0.88 kpc ("high v gas" in Figure 8) based on the detection of high-velocity Ca II and Na I absorption in HD 36665 and HD 37318 was discussed in Section 1.

Figure 9 shows the absorption line velocities relative to the LSR as a function of each star's offset R from the center of the SNR. If the absorbing material is in spherical, homologous expansion, then the velocities should be confined within the curve

$$v = v_0\left(1 - \frac{R^2}{R_{\rm SNR}^2}\right)^{1/2} \tag{4}$$

where v_0 is the expansion velocity at R_{SNR}. Such curves are shown in Figure 9 for $v_0 = 100$, 150, and 200 km s^{-1} and

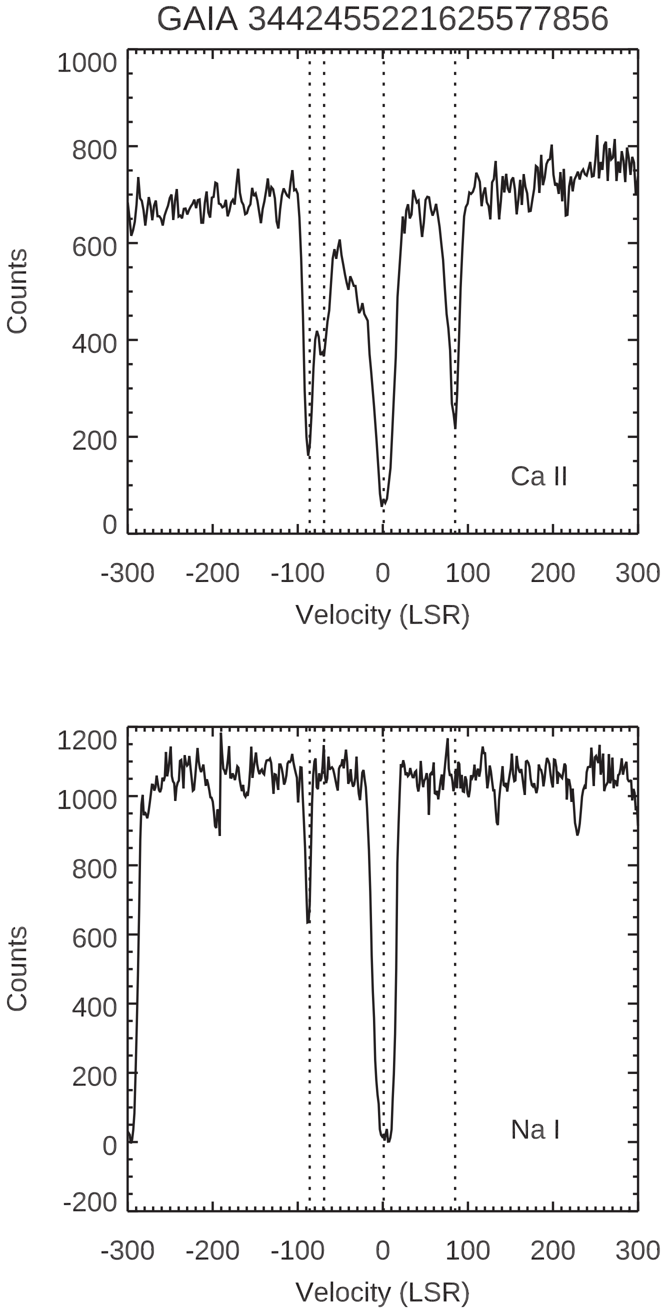

Figure 5. (Left): The Ca II and Na I spectra of the luminous blue star near the lower right corner of the selection box in Figure 1. This star has strong ISM absorption near zero velocity for both species. There are three additional strong Ca II absorption features at −86, −69, and +85 km s^{-1}, while only the feature at −86 km s^{-1} is seen in the Na I spectrum. The strong absorption line at −300 km s^{-1} in the lower panel is the D1 component of the Na I doublet associated with the D2 component at 0 km s^{-1}.

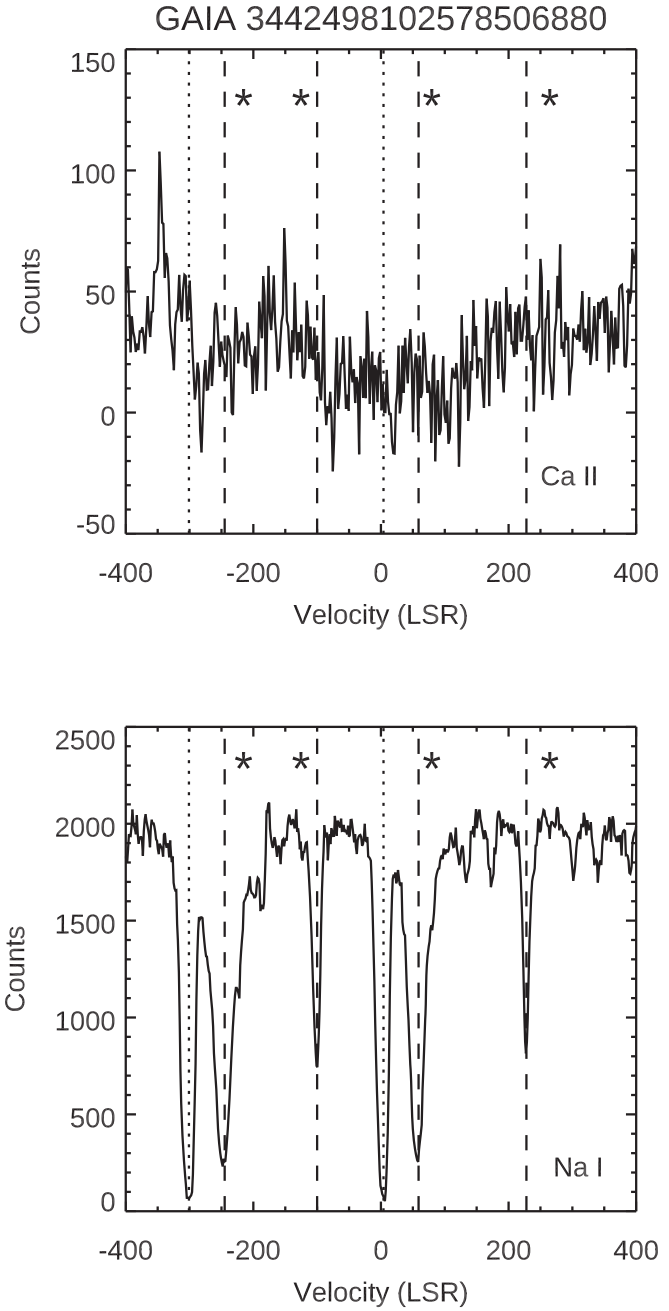

Figure 6. (Right): The Ca II and Na I spectra of the cool star just below the red clump in Figure 1. There are few counts in the Ca II spectrum because the star is a red giant. The high S/N Na I spectrum has strong interstellar absorption near 0 km s^{-1} but also strong stellar absorption lines at +59 km s^{-1} of multiple species including Na I, as labeled and marked by the dashed lines and asterisks. The strong absorption line at −300 km s^{-1} in the lower panel is the D1 component of the Na I doublet associated with the D2 component at 0 km s^{-1}.

$R_{\rm SNR} = 1\overset{\circ}{.}5$ (34 pc given our median distance estimate). If we adopt $v_0 = 150$ km s^{-1} and assume Sedov–Taylor expansion, then the age of the remnant is 94.6 ± 13.4 thousand years with $\log(E_{51}/n_1) = 0.36 \pm 0.16$, where E_{51} is the explosion energy in units of 10^{51} erg, n_0 is the ISM density in units of cm^{-3}, and we have assumed 10% errors on the radius and velocity. These are similar to the parameters proposed from the eROSITA X-ray observations of S146 (Michailidis et al. 2024). This age is moderately longer than the kinematic age estimated using the pulsar distance from the SNR center and its proper motion and significantly shorter than the pulsar spin-down age (33^{+17}_{-9} and 618 thousand years, respectively; Kramer et al. 2003). The low-ionization atomic Ca II and Na I states are expected only in the colder outermost shell of the SNR, and the complex emission-line morphology in Figure 2 suggests that the observed velocities may be subject to projection effects where we see a higher absorption column density along lines of sight perpendicular to shock fronts. This will tend to bias the observed absorption velocities to be lower than for a purely spherical expansion. Reich et al. (2003) suggested that the

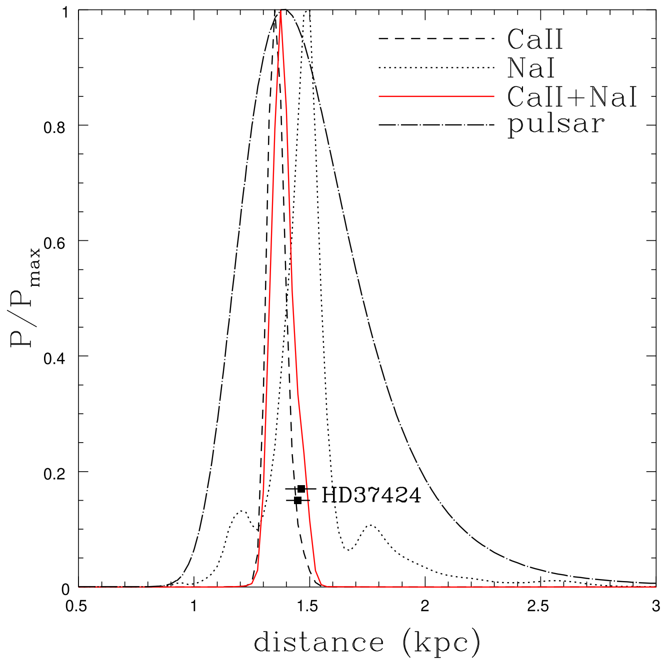

Figure 7. (Left): Normalized P/P_{max} probability distributions for the distance to S147 using only the Ca II (CaII, black dashed), only the Na I (NaI, black dotted), or both (CaII+NaI, red solid) absorption lines for an ISM velocity window of 2 ± 10 km s^{-1}. The black solid curve is the distance probability distribution implied by the pulsar parallax. The points show the Bailer-Jones et al. (2021) photometric (upper) and photogeometric (lower) distances to the candidate unbound binary companion HD 37424.

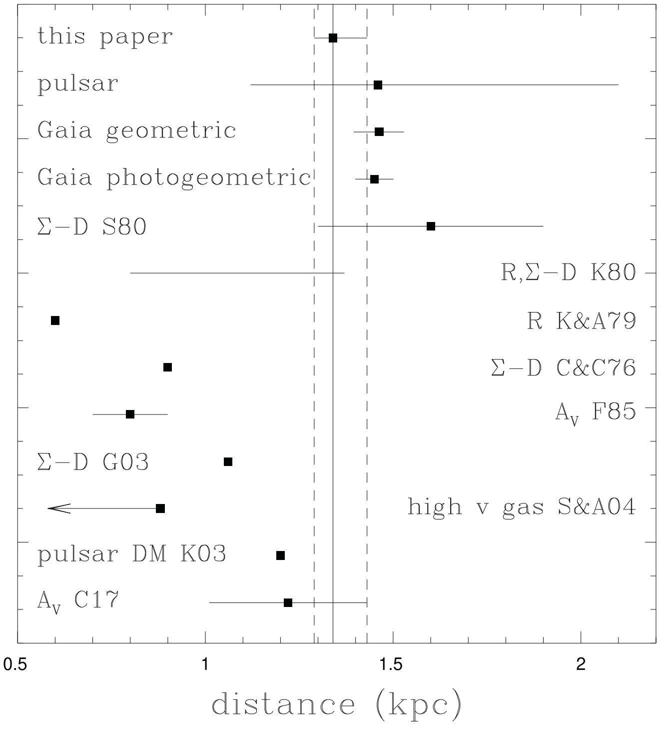

Figure 8. A comparison of distance estimates for S147 with our standard result at top, followed by the merged pulsar parallax distance (Ng et al. 2007; Chatterjee et al. 2009) and the Bailer-Jones et al. (2021) distance estimates for HD 37424. The other estimates use the radio surface brightness–diameter relation (Σ-D), models of the SNR radius (R), extinction (A_V), the pulsar dispersion measure (pulsar DM), and the high-velocity absorption discussed in Section 1 (high v gas). The references are K80 (Kundu et al. 1980), K&A79 (Kirshner & Arnold 1979), C&C76 (Clark & Caswell 1976), F85 (Fesen et al. 1985), G03 (Guseinov et al. 2003), S&A04 (Sallmen & Welsh 2004), K03 (Kramer et al. 2003), and C17 (Chen et al. 2017).

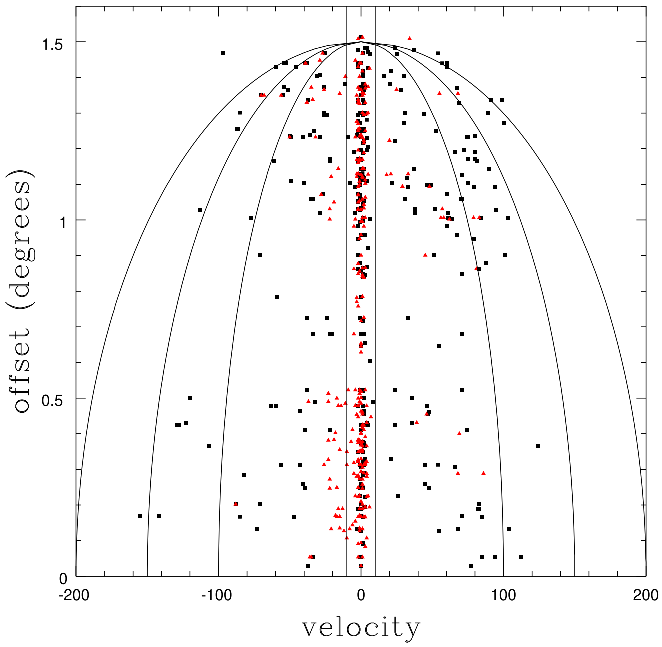

Figure 9. (Right): Absorption velocities relative to the LSR as a function of offset from the center of the SNR. The curves show the maximum expected velocities (Equation (4)) for an SNR radius of $R_{SNR} = 1\overset{\circ}{.}5$ and velocities at the edge of $v_0 = 100$, 150, and 200 km s^{-1}. The median 2 km s^{-1} LSR velocity has been subtracted.

discrepancy between the kinematic age estimated from the pulsar and the significantly longer ages derived from the size and expansion velocity of the SNR could be reconciled if the supernova exploded into a low-density wind bubble and so initially expanded more rapidly than estimates from Sedov–Taylor expansion into a uniform medium. This hypothesis works in the hydrodynamic simulations of Khabibullin et al. (2024).

Finally, we looked for correlations between the presence of high-velocity absorption lines and the SNR radio and emission-line fluxes. Unfortunately, there is no sufficiently deep, publicly available X-ray image of S147 (the eROSITA image of Michailidis et al. (2024) is probably suitable, but it is not public). For Hα we first tried the map from Finkbeiner (2003), which has the limitation that its resolution is only 6’. We were serendipitously contacted by an astrophotographer (C. Mauche) who had just generated an Hα and O [III] image of S147 using a ZWO ASI29MC Pro camera and a HUTECH/IDAS NBZ UHS dual narrowband filter. The stars were removed by an artificial intelligence application in `StarNetV2`, and the image was binned to 18″. We used the 1′ resolution 1.4 GHz map from the Canadian Galactic Plane Survey (CGPS; Taylor et al. 2003). Figures 2 and 3 show the dual emission-line and radio images with the three Hectospec fields and the target stars coded by whether they are background stars with high-velocity absorption, or background stars without high-velocity absorption.

Figures 10 and 11 show the normalized emission-line and radio flux distributions for each class of stars. The distributions in the emission-line flux for the background stars with and without high-velocity absorption are strikingly different—stars with high-velocity absorption are correlated with brighter line emission. The distribution of the foreground stars then lies between the two background star distributions as expected. The

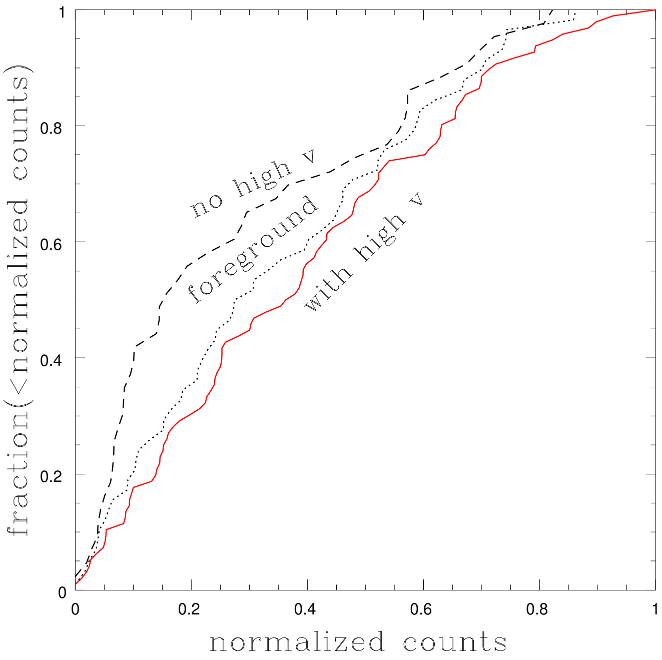

Figure 10. (Left): Integral distributions of the background stars with high-velocity absorption (solid red) and without high-velocity absorption (dashed black) in normalized counts from the emission-line image in Figure 2. The dotted curve shows the distribution of the foreground stars. The Kolmogorov–Smirnov test probability that the two background distributions are the same is 1.5%.

Kolmogorov–Smirnov test likelihood that the two background distributions are drawn from the same distribution is 1.5%. The emission-line image in Figure 2 was obtained as an astrophotography project and so is not a clean Hα or O [III] image. However, if we use the well-defined, but much lower resolution Finkbeiner (2003) Hα image, we find the same result. The distributions are similar to Figure 10, but the Kolmogorov–Smirnov significance of the differences is 21%, almost certainly due to the much lower resolution. For the normalized radio flux distribution in Figure 11, we removed stars too close to the numerous point sources seen in Figure 3. While the resulting flux distributions in Figure 11 show the same basic ordering as the emission-line flux distributions in Figure 10, the differences are far smaller, and the Kolmogorov–Smirnov significance is only 53%.

4. Discussion

We believe that the idea of Cha et al. (1999) for the Vela SNR that the appearance of high-velocity Ca II and Na I in stars as a function distance can be used to determine the distance to SNRs is now well validated by this work. We obtained a distance to S147 of 1.37 kpc (1.30–1.47 at 90% confidence), consistent with the less precise pulsar parallax and the parallax of the candidate unbound binary companion to the SN progenitor. As seen in Figure 2, we obtained only one partial and two complete Hectospec pointings covering only ∼20% of the remnant, so it would be easy to improve the statistics (Figures 4 and 7), to improve the kinematics of the SNR (Figure 9), or to better study correlations between the absorption lines and other properties of the SNR (Figures 10 and 11).

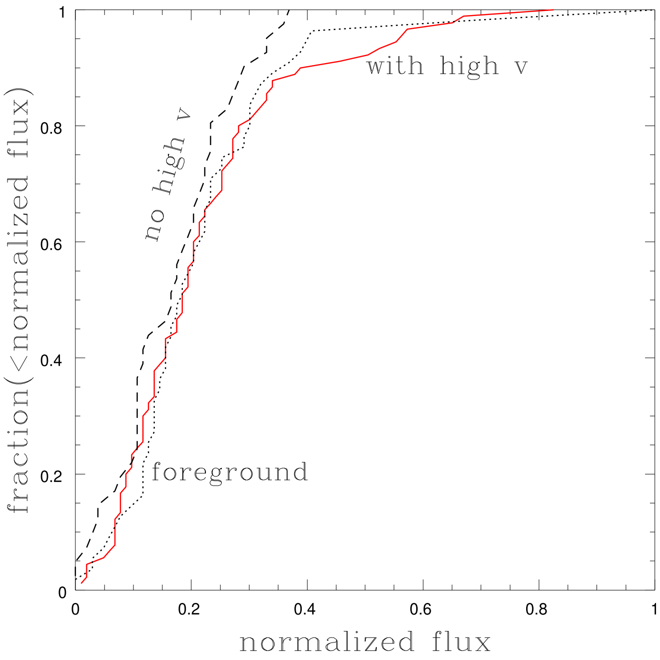

Figure 11. (Right): Integral distributions of the background stars with high-velocity absorption (solid red) and without high-velocity absorption (dashed black) in normalized flux from the 1.4 GHz image in Figure 3. The dotted curve shows the distribution of the foreground stars. The Kolmogorov–Smirnov test probability that the two background distributions are the same is 53%.

One of our goals was to determine which absorption lines were better for this method, and it appears to clearly be the Ca II lines. Of the 259 luminous hot stars observed ($M_G < 1.5$ mag, $B_P - R_P < 0.4$ mag), 101 showed high-velocity Ca II absorption lines, and only 60 showed high-velocity Na I absorption. The Ca II absorption velocities were also systematically higher, with a median velocity after excluding the ISM lines of 58 km s^{-1} relative to the LSR versus 25 km s^{-1} for Na I. This is a result of needing higher total column densities to detect Na I than Ca II because Na I is easily photoionized by near-UV photons below 2400 Å, while Ca II requires photons shortward of 1045 Å. Ca II and Na I originate in radiative shock waves in the outer layers of the SNR (Cox 1972a). Projection effects lead to lower column densities and higher velocities normal to the shock front and the reverse parallel to the shock front. This means that an absorption feature requiring a higher column density will be biased toward lower average velocities. While Ca II shows more and stronger absorption, it has the disadvantage of a bluer wavelength (3934/3968 Å versus 5890/5896 Å for Na I), where extinction losses are higher and spectrographs/detectors tend to be less efficient.

We focused on luminous hot stars because they lack stellar Na I and Ca II absorption (and narrow stellar absorption features generally) due to their temperatures. This greatly simplifies identifying absorption lines from the ISM and SNR. It is possible to apply this method to Na I absorption in the more numerous luminous red stars, but it is complicated by the stellar absorption features of Na I and many other species, as seen in Figure 6. Essentially, the stellar spectrum has to be modeled to confidently distinguish interstellar and stellar absorption features. This is almost certainly feasible but beyond our present scope. Being able to apply this method to luminous red giants will be increasingly important for SNRs with higher extinctions.

In old SNRs such as S147, we expected strong correlations between the Ca II and Na I column and the Hα and radio fluxes. The radiative shock waves responsible for the Ca II and Na I also drive the Hα emission (Cox 1972b), and the brightest radio flux in old SNRs originates in radiative shocks where the cooling post-shock gas compresses both the ambient cosmic-ray electrons and the magnetic field (van der Laan 1962; Raymond et al. 2020a; Tutone et al. 2021). We correlated the background stars with and without high-velocity absorption lines with emission-line and radio images of S147. We found a significant correlation of high-velocity absorption with the flux in an Hα/O [III] astrophotography image of S147 and, more weakly, with the far lower resolution Hα image from Finkbeiner (2003). This suggests that using emission-line maps to prioritize targets is likely more important than our center-versus-edge experiment. We found no significant correlation between the background stars with high-velocity absorption lines and the Canadian Galactic Plane Survey (Taylor et al. 2003) 1.4 GHz radio map of S147. The insignificant correlation with the radio emission may be driven by a combination of the modest $(1')$ resolution and limited dynamic range of the CGPS radio map for the emission from the SNR. Unfortunately, no sufficiently deep, publicly available X-ray image of S147 was available to check for correlations.

Based on these results, we initiated a program to obtain data for up to 16 additional Northern and Southern SNRs using MMT/Hectospec and Magellan/M2FS in the first trimester of 2024. As emphasized in the introduction, modern multifiber echelle spectrographs allow these observations to be carried out very efficiently. The selection of target stars for this trimester is not making use of the correlation between the existence of high-velocity absorption and emission-line flux we find here but will certainly serve to confirm the correlation for use in future observations. We are also investigating modeling the spectra of the red giants, which are currently just used to fill otherwise unused fibers, to also use them in the search for absorption features of SNRs.

Acknowledgments

We thank Christopher Mauche for sharing his images of S147 with us. We also had helpful discussions regarding sodium absorption with Jesse Han. C.S.K. is supported by NSF grants AST-1908570 and AST-2307385. Observations reported here were obtained at the MMT Observatory, a joint facility of the Smithsonian Institution and the University of Arizona. Data were reduced by the SAO TDC; we thank Sean Moran and Jaehyon Rhee for their help in that work.

Facility: MMT.

ORCID iDs

C. S. Kochanek https://orcid.org/0000-0001-6017-2961
John C. Raymond https://orcid.org/0000-0002-7868-1622
Nelson Caldwell https://orcid.org/0000-0003-2352-3202

References

Badenes, C., Harris, J., Zaritsky, D., & Prieto, J. L. 2009, ApJ, 700, 727
Bailer-Jones, C. A. L., Rybizki, J., Fouesneau, M., Demleitner, M., & Andrae, R. 2021, AJ, 161, 147
Blundell, K. M., & Bowler, M. G. 2004, ApJL, 616, L159
Bovy, J., Rix, H.-W., Green, G. M., Schlafly, E. F., & Finkbeiner, D. P. 2016, ApJ, 818, 130
Braun, C., Safi-Harb, S., Fryer, C. L., & Zhou, P. 2023, MNRAS, 525, 6257
Bressan, A., Marigo, P., Girardi, L., et al. 2012, MNRAS, 427, 127
Cha, A. N., Sembach, K. R., & Danks, A. C. 1999, ApJL, 515, L25
Chatterjee, S., Brisken, W. F., Vlemmings, W. H. T., et al. 2009, ApJ, 698, 250
Chen, B. Q., Liu, X. W., Ren, J. J., et al. 2017, MNRAS, 472, 3924
Clark, D. H., & Caswell, J. L. 1976, MNRAS, 174, 267
Corbet, R. H. D., Cheung, C. C., Kerr, M., et al. 2011, ATel, 3221, 1
Cox, D. P. 1972a, ApJ, 178, 143
Cox, D. P. 1972b, ApJ, 178, 159
Dinçel, B., Neuhäuser, R., Yerli, S. K., et al. 2015, MNRAS, 448, 3196
Dodson, R., Legge, D., Reynolds, J. E., & McCulloch, P. M. 2003, ApJ, 596, 1137
Drimmel, R., Cabrera-Lavers, A., & López-Corredoira, M. 2003, A&A, 409, 205
Dubner, G., & Giacani, E. 2015, A&ARv, 23, 3
Fabricant, D., Fata, R., Roll, J., et al. 2005, PASP, 117, 1411
Fesen, R. A., Blair, W. P., & Kirshner, R. P. 1985, ApJ, 292, 29
Fesen, R. A., Neustadt, J. M. M., Black, C. S., & Milisavljevic, D. 2018, MNRAS, 475, 3996
Fesen, R. A., Weil, K. E., Cisneros, I., Blair, W. P., & Raymond, J. C. 2021, MNRAS, 507, 244
Finkbeiner, D. P. 2003, ApJS, 146, 407
Fraser, M., & Boubert, D. 2019, ApJ, 871, 92
Gaia Collaboration, Prusti, T., de Bruijne, J. H. J., et al. 2016, A&A, 595, A1
Gaia Collaboration, Vallenari, A., Brown, A. G. A., et al. 2023, A&A, 674, A1
Green, D. A. 2009, BASI, 37, 45
Green, D. A. 2019, JApA, 40, 36
Green, G. M., Schlafly, E. F., Finkbeiner, D. P., et al. 2015, ApJ, 810, 2525
Guseinov, O. H., Ankay, A., Sezer, A., & Tagieva, S. O. 2003, A&AT, 22, 273
Hinton, J. A., Skilton, J. L., Funk, S., et al. 2009, ApJL, 690, L101
Jennings, Z. G., Williams, B. F., Murphy, J. W., et al. 2014, ApJ, 795, 170
Kameswara Rao, N., Lambert, D. L., Reddy, A. B. S., et al. 2020, MNRAS, 493, 497
Kerzendorf, W. E., Schmidt, B. P., Asplund, M., et al. 2009, ApJ, 701, 1665
Khabibullin, I. I., Churazov, E. M., Chugai, N. N., et al. 2024, arXiv:2401.17261
Kirshner, R. P., & Arnold, C. N. 1979, ApJ, 229, 147
Kochanek, C. S. 2021, MNRAS, 507, 5832
Kochanek, C. S. 2022, MNRAS, 511, 3428
Kochanek, C. S., Auchettl, K., & Belczynski, K. 2019, MNRAS, 485, 5394
Kramer, M., Lyne, A. G., Hobbs, G., et al. 2003, ApJL, 593, L31
Kundu, M. R., Angerhofer, P. E., Fuerst, E., & Hirth, W. 1980, A&A, 92, 225
Lin, R., van Kerkwijk, M. H., Kirsten, F., Pen, U.-L., & Deller, A. T. 2023, ApJ, 952, 161
Margon, B. 1984, ARA&A, 22, 507
Marigo, P., Bressan, A., Nanni, A., Girardi, L., & Pumo, M. L. 2013, MNRAS, 434, 488
Marshall, D. J., Robin, A. C., Reylé, C., Schultheis, M., & Picaud, S. 2006, A&A, 453, 635
Mateo, M., Bailey, J. I., Crane, J., et al. 2012, Proc. SPIE, 8446, 84464Y
Michailidis, M., Pühlhofer, G., Becker, W., et al. 2024, arXiv:2401.17312
Ng, C. Y., Romani, R. W., Brisken, W. F., Chatterjee, S., & Kramer, M. 2007, ApJ, 654, 487
Pasquini, L., Avila, G., Allaert, E., et al. 2000, Proc. SPIE, 4008, 129
Pastorelli, G., Marigo, P., Girardi, L., et al. 2020, MNRAS, 498, 3283
Perryman, M. A. C., Lindegren, L., Kovalevsky, J., et al. 1997, A&A, 323, L49
Phillips, A. P., & Gondhalekar, P. M. 1983, MNRAS, 202, 483
Phillips, A. P., Gondhalekar, P. M., & Blades, J. C. 1981, MNRAS, 195, 485
Raymond, J. C., Chilingarian, I. V., Blair, W. P., et al. 2020a, ApJ, 894, 108
Raymond, J. C., Slavin, J. D., Blair, W. P., et al. 2020b, ApJ, 903, 2
Reich, W., Zhang, X., & Fürst, E. 2003, A&A, 408, 961
Ren, J.-J., Liu, X.-W., Chen, B.-Q., et al. 2018, RAA, 18, 111
Ritchey, A. M., Federman, S. R., & Lambert, D. L. 2024, MNRAS, 528, 4490
Sallmen, S., & Welsh, B. Y. 2004, A&A, 426, 555
Sheinis, A. I. 2016, Proc. SPIE, 9908, 99081C
Silk, J., & Wallerstein, G. 1973, ApJ, 181, 799
Sofue, Y., Furst, E., & Hirth, W. 1980, PASJ, 32, 1
Szentgyorgyi, A., Furesz, G., Cheimets, P., et al. 2011, PASP, 123, 1188
Taylor, A. R., Gibson, S. J., Peracaula, M., et al. 2003, AJ, 125, 3145
Temim, T., Slane, P., Raymond, J. C., et al. 2022, ApJ, 932, 26
Tutone, A., Ballet, J., Acero, F., D'Aì, A., & Cusumano, G. 2021, A&A, 656, A139
van den Bergh, S., Marscher, A. P., & Terzian, Y. 1973, ApJS, 26, 19
van der Laan, H. 1962, MNRAS, 124, 125
Vink, J. 2012, A&ARv, 20, 49